

**Near Grazing Scattering from Gaussian Rough Surfaces:
Numerical Results**

Ernesto Rodríguez and Yunjin Kim
Jet Propulsion Laboratory
California Institute of Technology
4800 Oak Grove Dr., Pasadena, CA 91109

Abstract: We examine the behavior of the scattered electromagnetic field from random Gaussian power-law surfaces for near grazing incidence. Using the method of moments and periodic boundary conditions, we calculate the bistatic cross section for both polarizations and a variety of surface heights and slopes for incidence angles as large as 89° . We examine the results to elucidate the scattering mechanism which dominates at these high grazing angles and find evidence for Bragg scattering as well as shadowing effects and surface modes. The polarimetric behavior of the field is discussed in detail.

1. Introduction

While the main physical mechanisms for moderate incidence angle scattering from rough surfaces are qualitatively understood (although we still lack a theory which gives good quantitative results for all surfaces), the same cannot be said for scattering near grazing incidence. We know that shadowing must play some role, but we do not know how to derive a shadowing correction from first principles. There are some near grazing data from the ocean surface (see Wetzel [1990] and Trizna [1991] for a review) but with ocean surface data it is hard to be sure that the surface is adequately characterized at the appropriate length scales. Ocean data seems to indicate that the small perturbation method (SPM) [Rice, 1951] provides unexpectedly good predictions for vertical polarization, but not for horizontal polarization. It has been observed that the ocean horizontal cross section can be as large as the vertical one, and that the returns can exhibit highly intermittent behavior. A connection of these observations to shadowing or feature scattering has been suggested [Wetzel, 1990]. In spite of these pieces of information, we still do not have a clear physical understanding of the general scattering mechanisms in operation, or whether such a thing exists.

One of the problems with trying to disentangle these clues is that we do not know if present scattering theories (after, perhaps, being corrected for shadowing effects) are adequate and the surfaces are insufficiently characterized; or whether these theories are fundamentally wrong in this incidence regime. The purpose of this paper is to help elucidate this question by presenting the results of numerical scattering calculations at small grazing

incidence for various surface heights, slopes, and polarizations and to describe the behavior of the scattered field as these quantities are varied. The emphasis of this paper will be in the presentation of the numerical results and a discussion of the physical scattering mechanisms which can be inferred from these results.

To this end, we have implemented a periodic boundary condition version of the method of moments (MOM) which allows us to avoid edge current effects which have restricted the application of this method to small grazing angle incidence. The numerical implementation of this method is presented in the next section and Appendix A. The following three sections are devoted to studying the far field polarimetric response, the surface current, and shadowing and near field effects. The detailed comparison of these results against analytic theories will be given elsewhere, although we present some qualitative discussions of this topic. The present work extends previous work by Thorsos [1990] and Ngo and Rino [1993] by examining the incidence angle beyond 80° , and by giving a fully polarimetric treatment of the scattered field [Michelet et al., 1992].

2. Numerical Implementation

The numerical implementation of the scattering calculations consisted in generating ensembles of Gaussian rough surfaces; using the method of moments (MOM) to calculate the surface current; calculating the scattered field modes; and, finally, deriving the average polarimetric signature by averaging over the ensemble. Due to computational limitations, we restricted ourselves to one-dimensional perfectly conducting surfaces.

The random surfaces were generated by making an uncorrelated, unit variance, Gaussian random noise sequence in the wavenumber domain, applying the appropriate filter function, and Fourier transforming to the coordinate domain (for details, see [Rodriguez, et al., 1992]). The surface spectrum was proportional to κ^{-s} , and we examined a spectral decay of $s = 3$. This spectral decay is observed in ocean surfaces. We also examined a spectral decay of $s = 2.5$ but do not show the results here since the conclusions drawn from them are similar to the $s = 3$ case. The smallest wavelength present in these surfaces was 0.2λ , where λ is the electromagnetic wavelength. The longest wavelength, A , was varied to examine

the effects of changing the correlation length (or the surface slope to height ratio). We examined the longest wavelengths of 102.4λ , 51.2λ , 25.6λ , and 12.8λ . Three surface root mean squared (rms) heights were examined: 1λ , 0.5λ , and 0.1λ but we do not present the 0.5λ results since they add nothing of consequence. Figure 1 presents the surface slopes and curvatures for the $s=3$ surfaces, as well as the fraction of the surface which is in monostatic shadowing for various two-scale high frequency shadowing cut-offs. Two-scale shadowing is implemented by calculating the shadowed area after the high frequency components above the cut-off frequency are removed. As can be seen, a substantial fraction of the surface is shadowed for the larger surface heights, even when the two-scale shadowing cut-off is set to 5λ .

The biggest problem encountered in MOM calculations from random rough surfaces is the avoidance of edge effects. This problem was recognized long ago by Axline and Fung [1978] and various methods have been proposed to deal with it. Currently, the most popular method in the literature is the tapered wave method introduced by Thorsos [1988], where the incident field is taken to be a tapered field which satisfies Maxwell's equations approximately, but attenuates the return from the edges so they are negligible. While this method is very attractive from the numerical standpoint, it is limited by the validity of the tapering approximation. Thorsos [1988] has shown that the approximation is valid as long as the parameter $\epsilon = \lambda/L \cos \theta_0 \ll 1$, (In this expression, L is the surface length, and θ_0 is the incidence angle.) It is clear that, as $\theta_0 \rightarrow \pi/2$ one must have $L \rightarrow \infty$ for the parameter to remain small. This makes the method unsuitable for near grazing calculations, although Ngo and Rino [1993] have extended the validity of the method to approximately 80° .

An alternate way of avoiding edge effects is to assume that the surface is periodic and that the period is large enough so that the scattered field, which now has a discrete angular spectrum, approximates the continuous spectrum from an infinite surface. This will be true if the angular separation between modes is smaller than the angular resolution required to observe the surface. This method was proposed by us [Rodriguez et al., 1992] [Kim et al., 1992] to deal with moderate incidence angles and the reader is referred there for our

conventions. The key to implementing this method is the evaluation of the periodic Green's function and its normal derivative on the surface. In the work cited above, we approximated the Green's function by summing only a few terms of its infinite series representation. While this is adequate for moderate incidence angles, it is not sufficient as the incidence angle approaches grazing. Here, we make use of an integral representation of the periodic Green's function obtained by Veysoglu et al. [1991] together with some approximations which make the Monte Carlo evaluation computationally efficient. The details of the numerical method are presented in Appendix A.

We used the expressions for the Green's function obtained in Appendix A together with the MOM. For each case studied, we used a total of 100 Monte Carlo realizations and all the calculations were performed using double precision arithmetic. The energy conservation was calculated for each case and was found to be better than 0.1% in all cases, and better than 0.001% in most cases. We estimate that the error bars in our scattering results due to speckle are of the order of ± 1 dB.

3. Far Field Results

For one dimensional surfaces, the complete polarimetric Stokes matrix has only four non-zero elements [Michel et al., 1992]. Rather than using the Stokes matrix elements, in this paper we will examine the following parameters which contain the same information but are easier to interpret physically:

$$\sigma_0^{(V)}(\theta_n) = kL \cos^2 \theta_n \langle E_V(\theta_n) E_V^*(\theta_n) \rangle \quad (1)$$

$$\sigma_0^{(H)}(\theta_n) = kL \cos^2 \theta_n \langle E_H(\theta_n) E_H^*(\theta_n) \rangle \quad (2)$$

$$\gamma(\theta_n) = \frac{|\langle E_V(\theta_n) E_H^*(\theta_n) \rangle|}{\sqrt{\langle |E_H(\theta_n)|^2 \rangle \langle |E_V(\theta_n)|^2 \rangle}} \quad (3)$$

$$\Phi(\theta_n) = \text{Arg}(\langle E_V(\theta_n) E_H^*(\theta_n) \rangle) \quad (4)$$

where θ_n is the scattering angle for the n th propagating mode and is given by the grating equation

$$\sin \theta_n = \sin \theta_0 + \frac{n}{L/\lambda} \quad (5)$$

$E_H(\theta_n)$ and $E_V(\theta_n)$ are, respectively, the horizontal and vertically polarized scattering modes, and we have normalized the bistatic cross sections such that it agrees with nonperiodic surface case after integrating over all scattering angles [Lou et al., 1991]. The parameters γ and Φ represent the magnitude of the field correlation and the relative phase difference between the H- and V-polarized fields. In the Small Perturbation Method (SPM) or Physical Optics limits the correlation should be unity and the H and V fields should be out of phase by 180° . Deviations from these values can be due to two causes: a different scattering mechanism (such as multiple scattering or shadowing) applies; or, the surface features responsible for producing the scattering are different for the two polarizations.

We examine first the small surface height limit. The expansion parameter for the SPM is given by $\delta = k\sigma_h \cos \theta_0$, where σ_h is the surface height standard deviation, and we expect that SPM will always apply for small surface heights provided the surface slope is small, which is the other assumption made in deriving the SPM results. Figure 2 presents the results for the four polarimetric parameters for an incidence angle of 89° and $\sigma_h = 0.1\lambda$. These results are what is expected when SPM holds: the bistatic cross section is (aside from an angular factor) a reflection of the magnitude of the Bragg wavenumber Fourier component. For the two surfaces whose longest wavelengths are 51.2λ and 25.6λ , there are no resonant Bragg waves close to the forward direction and the bistatic cross section shows a severe drop for these angles. The small contribution in this direction can be attributed to non-Bragg or multiple scattering. With the exception of these angles, and of the near grazing mode in the backward direction, the field correlation is unity. The one deviation from the expected SPM behavior is shown by the HV relative phase difference which decreases to 170° for the surface with the highest slope variance. Also, notice that the phase difference for the angles where single Bragg scatter is not supported shifts radically. This is consistent with the multiple scattering interpretation for the mechanism: a double bounce event has $\Phi = 0$ in the physical optics limit. The results for an incidence angle of 80° (not shown) are similar, but in that case the discrepancies in the correlation coefficient and the phase shift in the single Bragg scatter region are not present indicating that at this incidence angle

SPM holds even better.

Next, we examine the large surface limit, $k\sigma_L \equiv 2\pi$. Notice that if we are to take δ as the sole guide for the applicability of SPM, we should expect SPM results are good very near grazing, independent of the surface height or the surface slope. Figure 3 shows the scattering results for an incidence angle of 80° and four surface types. Notice that the smoother surfaces still behave close to the way expected from SPM. The major departures from this assumption are in the HV phase difference, which is now close to 160° for all angles, and in the correlation coefficient, which decreases away from the specular direction.

More interesting behavior is observed for the surfaces with the higher slopes. First of all, the backscatter cross section increases dramatically in the backward direction. In the forward direction, vertical and horizontal polarizations show very different behavior. As the surface slope increases the vertically polarized energy in the forward and nearby directions decreases dramatically. For horizontal polarization, on the other hand, the decrease is much smaller in the coherent direction although we have shown that this energy is in fact not coherent by calculating the coherent component and seeing that it does not follow this trend.

We also notice that the angles near the forward direction, where no single Bragg scattering exists are now completely filled, suggesting the presence of multiple scattering. This surprise is reinforced when we examine the HV phase difference for these angles: for the roughest surfaces the phase difference approaches zero, even in the forward direction, indicating that for these angles multiple scattering is the dominant mechanism. This is corroborated also by the correlation coefficient which decreases dramatically near the forward direction.

For the other scattering angles, we notice the HV phase difference is very close to 160° , almost independently of the surface slope. The correlation coefficient also tends to drop in the backward direction indicating that the H and V sources may be different in these directions. As we will argue below, this may be due to the different behavior of the field in the shadow zones and in its coupling to surface waves.

Figure 4 presents similar results for an incidence angle of 89.0° , indicating that the scattering behavior observed here is not a strong function of the additional shadowing encountered as the angle approaches grazing. To further examine the source of the scattering we tried to isolate the single Bragg scatter contribution by filtering the surface in such a way that no resonant Bragg components existed for scattering angles smaller than 0° . Figure 5 shows the results. Up to 0° , the cross sections remain unaltered, but for negative angles there is a dramatic drop of two orders of magnitude in the scattered energy. This seems to indicate that, while SPM is not accurate, Bragg resonance is still the dominant scattering mechanism in these directions. Notice also that the drop-off occurs less suddenly for the rougher surface indicating that resonance with wavenumbers near the Bragg wavenumber is important as the surface slope increases. This is also a feature of the unified perturbation method (UPM) [Rodríguez and Kim, 1992], and of two-scale theories in general.

4. Surface Current Results

An advantage of solving the scattering problem numerically is that one obtains the surface current (11) (12) as a byproduct. In this section we examine the current to gain further insight into the scattering mechanism near grazing. However, rather than analyzing the surface current directly, we examine a related quantity, which we call the source function and define it as

$$\tilde{F} = \frac{\eta_0}{2} \left[1 + (\nabla \xi)^2 \right]^{1/2} \exp[-i(\vec{\kappa}_0 \cdot \vec{\rho} - p_0 \xi)] \tilde{J} \quad (6)$$

where \tilde{J} is the surface current; κ_0 and $-p_0$ are the horizontal and vertical components of the incident wavevector, respectively; and η_0 is the impedance of free space. By removing the phase (6) (11), we have obtained a quantity whose Fourier transform,

$$F_\gamma = \int dx \exp[-i\gamma x] F(x)$$

can be related to the surface spectrum according to Suhl and UPM. In the previous equation, we have taken the source function in one dimension, as appropriate for one dimensional numerical experiments. As motivation for the following results, we present the results obtained for the spectrum of the source function according to first order UPM.

For horizontal polarization, the spectrum of the UPM source function is given by

$$\langle E_\gamma^* E_\gamma^* \rangle = 2\pi \cos \theta_0 \delta(\gamma)^2 + W(\gamma) \cos^2 \theta_0 |p(\gamma) - p_0|^2 \quad (7)$$

where $p(\gamma) = (k^2 - (\kappa_0 + \gamma)^2)^{1/2}$ is the vertical component of the propagation wavevector, and $W(\gamma)$ is the surface height spectrum at wavenumber γ . The term containing the square of the delta function is due to the coherent current. Notice that the other term is proportional to the surface spectrum and vanishes when $p(\gamma) = p_0$; i.e. for wavenumbers corresponding to the coherent and backscattered directions.

For vertical polarization, the spectrum of the UPM source function is

$$\langle E_\gamma^* E_\gamma^* \rangle = (2\pi \delta(\gamma)^2 + V/\gamma) \left[|p(\gamma) - p_0|^2 + 2\gamma^2 \operatorname{Re} \left(\frac{p(\gamma) - p_0}{p(\gamma)} \right) \gamma^2 \frac{(\kappa_0 + \gamma)^2 + |p(\gamma)|^2}{|p(\gamma)|^2} \right] \quad (8)$$

Notice that, in contrast to horizontal polarization, this expression exhibits a singularity which is integrable on the field when there exists coupling to surface waves; i.e., when $p(\gamma) \neq 0$. It will be of interest to see from the numerical results whether the source function is strongly peaked at this wavenumber indicating that this type of coupling is physical rather than an artifact of the perturbation solution. In addition to these results both SPM and UPM predict (to the degree of approximation used here) perfect correlation between the H and V source functions since they are both proportional to the Fourier transform of the surface height only, and zero phase difference for the wavelengths corresponding to propagating modes.

Figures 6a-c present the results for the spectrum of the source function for three surface types and an incidence angle of 89° . The average has been taken over 100 realizations. The coherent peak located at $\gamma = 0$ is clearly apparent for all three surface types and for both polarizations. For the smoothest surfaces, the horizontal polarization spectrum clearly shows a null at the expected wavenumber, i.e., when $p(\gamma) = p_0$, but as the roughness increases the null fills in, indicating possible multiple scattering contributions. For vertical polarization, on the other hand, the enhancement at the wavenumber appropriate for coupling to surface waves is clearly evident for all three surfaces indicating that this

type of coupling is a robust contributor to the scattering for all slopes. We notice that the correlation decreases with surface slopes and **that** the decrease is especially apparent for Bragg waves which couple in the backward direction. We also notice that the relative phase increases for these waves. This suggests that different scattering mechanisms are responsible for scattering in the backward direction for each polarization.

To further study the influence of the Bragg scattering mechanism, we compute the source function spectrum in Figures 7a-c for a surface whose Fourier components of Wavelength smaller than λ have been removed. For all the surfaces, the spectrum of the source function shows a dramatic fall-off for wavelengths smaller than the Bragg cutoff while remaining unchanged for the larger wavelengths. This gives a clear indication that even though the correlation and phase difference results do not match **exactly** with the expected SPM results, the Bragg resonant scattering mechanism is still the dominant scattering mechanism operating at $\pm 11^\circ$ incidence angles.

As an interesting feature, notice that the enhancement at $p(\gamma) = 0$ is still present for vertical polarization, even though the resonant waves have been removed. This is in qualitative agreement with the higher order predictions of UPM. Notice also that once the single scattering component is removed, there appear enhancements of the surface spectrum for wavelengths equal to $\lambda/4$. These enhancements are present for both horizontal and vertical polarizations and for the three surface types. We do not have an explanation for the behavior at this time.

5. Near Field and Shadowing Results

It is often hypothesized that shadowing plays a key role in determining the scattering behavior as the incidence angle approaches grazing. To examine this conjecture we looked at the amplitude of the surface current and the near field in areas which are known to be in the geometric shadow. Shadowing is a multiple scattering phenomenon and it is of interest to examine the structure of the near field in these areas. Furthermore, from the discussion above, we expect that the vertical polarization results will exhibit some sort of coupling to

localized surface waves. This coupling should be apparent if one examines the evanescent field.

The method of calculation using periodic boundary conditions offers the distinct advantage that the near field can be separated into its propagating and evanescent (as well as upward and downward) components. Figure 8 presents the horizontal polarization near and evanescent fields for a surface feature which causes deep shadowing. From the near field magnitude it is clear that the peak to the left is causing knife edge diffraction into the shadowed valley. A similar calculation (not presented here) shows that almost all of the field inside the shadowed valley is due to downward propagating waves, as one would expect from intuition: the peak current reradiates the appropriate field for the knife edge diffraction and to cause shadowing. In the region below the knife edge shadowing field, the deep shadow, the current magnitude decreases dramatically. It starts to increase in the knife edge diffraction area, although it is still in the geometric shadow. The evanescent field is strongest in the deep shadow area, where it is needed to extinguish the incident field. All tilt'HP observations agree well with our intuitive expectations. We also note that the current magnitude increases dramatically on the slopes pointing toward the transmitter and that most of the backward propagating field seems to emanate from these points of high slope. This implies that near grazing the scattering mechanism also depends strongly on the local slope, as well as on the presence of Bragg resonant waves. This is consistent with the results obtained in the previous sections.

Figure 9 presents the equivalent results for vertical polarization. We see that the knife edge diffraction is still present, as is the scattering in the backward direction due to the surface slopes. But, in contrast to the horizontal polarization case, the current decreases much less in the region of deep shadow. The transition should be slower is to be expected because the vertically polarized current cannot change abruptly in the horizontal direction and still satisfy the charge continuity equation, unlike its horizontal counterpart which flows into the page. However, this phenomenon is expected to last only a few wavelengths, not fifteen, as seen in the figure. What is apparent in the plot of the surface current is that in

the deep shadow region the surface current is dominated by a single frequency component whose wavelength is approximately half an electromagnetic wavelength. That a surface wave is indeed present can be seen in the evanescent field magnitude which exhibits modulations which closely correspond to the surface current and which has phase fronts in the vertical direction. The horizontal polarization results do not exhibit a similar phenomenon.

If the surface wave is due to strong coupling of the momentum to a particular surface wavenumber component, as predicted by UPM, for instance, we should expect that if that surface component is removed, the surface waves will be strongly attenuated. In Figure 10 we present the near field scattering results for a filtered version of the surface used in Figure 9. The filter has removed all surface components whose wavelength is smaller than λ . Figure 10 shows that, while many of the large scale features of the scattered field are common to both examples, the surface wave is strongly attenuated, as expected. This can also be seen by examining the surface current magnitude, which does not present the same rapid oscillations present in Figure 9.

The UPM results predict that, if the surface is rough enough, there will be a strong coupling to surface waves, even when the incidence angle is not near grazing. As a final test for the validity of the mechanism proposed above, we present in Figure 11 the near field results for the same surface used in Figure 9, but for an incidence angle of 60° . While the near field results are quite different for this case, the evanescent field still shows the presence of a surface wave, as does the surface current.

The example chosen here is for a very rough surface since this tends to enhance the shadowing phenomena. However, the phenomena discussed here are present for smaller surface slopes, but are correspondingly smaller.

6. conclusions

We presented calculations for scattering from power law rough surfaces at incidence angles very close to grazing incidence. For small surface heights, we showed that resonant single Bragg scattering dominates. As the surface height increases, we showed how the cross sections changed and argued for the presence of double bounce scattering close to the

forward direction. Although the scattered fields no longer have the typical SPM behavior, we found strong evidence that a Bragg resonant mechanism (which is quantitatively different from SPM) was still the dominant scattering mechanism. However, we also showed that, for the surfaces with the higher slopes, other mechanisms, such as shadowing, edge diffraction, or surface tilts, were also important. We found indications that in the vertically polarized case coupling to a surface mode was possible and showed that this is qualitatively consistent with predictions of perturbation theory. A more detailed comparison of the numerical results with analytical theories will be given elsewhere.

Appendix A

The periodic Green's function is given by [Tsang et al., 1986]

$$g_p(\vec{r}, \vec{r}') = \frac{i}{4} \sum_{m=-\infty}^{\infty} H_0^1 \left(k \sqrt{(x - (x' + mL))^2 + (z - z')^2} \right) \exp[imk \sin \theta_0 L] \quad (9)$$

Veisoglu et al. [1991] have evaluated the sum

$$S(a, b, r, s) \equiv \frac{i}{4} \sum_{m=-1}^{\infty} H_0^1 \left(\sqrt{s^2 (m + b)^2 + a^2} \right) \exp[imr] \quad (10)$$

$$= \frac{e^{ibs}}{\pi} e^{i(s+r)} \int_0^{\infty} du \frac{e^{-sbu^2}}{e^{su^2} - e^{-i(s+r)}} \frac{\cos(au\sqrt{u^2 - 2i})}{\sqrt{u^2 - 2i}} \quad (11)$$

where we use a slightly different notation from Veisoglu et al. to emphasize the symmetry properties of the sum

$$a = k(z - z') \quad (12)$$

$$b = -(x - x')/L \quad (13)$$

$$s = kL \quad (14)$$

$$r = -kL \sin \theta_0 \quad (15)$$

The integral is rapidly convergent and can be evaluated numerically. Given this sum, the periodic Green's function can be written as

$$g_p = \frac{i}{4} H_0^1 \left(\sqrt{(sbb)^2 + a^2} \right) + S(a, b, r, s) + S(a, -b, -r, s) \quad (16)$$

While the previous expression provides an exact evaluation of the periodic Green's function, it is not convenient for use in Monte Carlo applications. The function $S(a, b, r, s)$ depends on the surface height through the parameter a . This means that S must be numerically integrated as many times as the number of elements in the MOM matrix. For large surfaces, this is impractical since it makes the matrix loading the most computationally expensive part, by far. To overcome this problem, we will make use of the fact that we are interested in surfaces which are much longer than the electromagnetic wavelength. From the definition of $S(a, b, r, s)$, one can show that the following identity holds:

$$\frac{i}{4} \sum_{m=-1}^N H_0^1 \left(\sqrt{s^2 (m+b)^2 + a^2} \right) e^{imr} = S(a, b, s, r) - e^{iNr} S(a, N+b, r, s) \quad (17)$$

and the periodic Green's function can be written as

$$g_p = \frac{i}{4} \sum_{m=-N}^N H_0^1 \left(\sqrt{s^2 (m+b)^2 + a^2} \right) + e^{iNr} S(a, N+b, r, s) + e^{-iNr} S(a, N-b, -r, s) \quad (18)$$

Since $b \geq -1$, for long surfaces one will have that $s^2(2+b)^2 \gg a^2$, or, equivalently, that $1 \gg (h-h')^2/L^2$, where h is the surface height. When this is the case, the exponential in the integrand of S will dominate the value of the integral and the parameter a will only have a small influence. This allows us to expand S in terms of a

$$S(a, N+b, s, r) \approx \sum_{n=0}^{n_{max}} \frac{a^n S^{(n)}(0, N+b, s, r)}{n!} \quad (19)$$

where $S^{(n)}$ is the n th partial derivative of S with respect to a , and is easily obtained by differentiating equation (11). These integrals are also rapidly convergent and independent of the surface height so that they can be precomputed and stored in tables.

The numerical evaluation of the Green's function is performed by evaluating equation (18) and replacing S by its approximation, equation (19). In this paper, we have chosen the surface length to be 102.4λ and the surface is sampled at 0.1λ intervals. By comparing against the exact result we have found that it is sufficient to take $N = 1$, and $n_{max} = 6$. All the integrals, as well as all subsequent calculations, were computed with double precision arithmetic. There is no absolute test of the numerical accuracy of the

MC A results, but here are some necessary tests to which we subjected our results. Most importantly, we checked the degree of energy conservation: for all the results presented here, the energy conservation was better than 0.1%, and in most cases it was better than 0.001%. For selected surfaces, we also checked the periodicity of the surface current, the reciprocity of the scattered field, and the extinction of the field below the surface. All the results presented here satisfied these tests to a good accuracy.

For the vertical polarization calculations, it is necessary to compute the normal derivative of the Green's function at the surface. Using the previous results, we obtain the following expression

$$\begin{aligned} \hat{n} \cdot \nabla g_p = & \frac{i}{4} \sum_{m=-N}^N H_1^1 \left(\sqrt{s^2 - m^2} (b)^2 + a^2 \right) - \frac{a + h_x s(m + b)}{\sqrt{s^2 (m + b)^2 + a^2}} \\ & + N_r Q(a, N + b, r, s, h_x) + e^{-iN_r} Q(a, N - b, -r, s, h_x) \end{aligned} \quad (20)$$

where h_x is the surface slope, and

$$\begin{aligned} Q(a, b, r, s, h_x) = & k_z \frac{e^{i h_x s}}{\pi} e^{i(s+r)} \int_0^\infty du \frac{e^{-sbu^2}}{e^{su^2} - e^{-i(s+r)}} \\ & \left[-\frac{h_x (u^2 - i) \cos \left(au\sqrt{u^2 - 2i} \right)}{\sqrt{u^2 - 2i}} + u \sin \left(au\sqrt{u^2 - 2i} \right) \right] \end{aligned} \quad (2)$$

This expression is evaluated, in analogy with the expression for the periodic Green's function, by expanding Q in powers of a to sixth order

Acknowledgements

The research described in this paper was performed by the Jet Propulsion Laboratory, California Institute of Technology, under contract with the Office of Naval Research.

References

- Axline, R.M., and A.K. Fung, "Numerical computation of scattering from a perfectly conducting random surface," IEEE Trans. Antennas Propag., AP-26, 482-488, 1978.

- Kim, Y., E. Rodríguez , and S.L. Durden, "A numerical assessment of rough surface scattering theories: vertical polarization," *Radio Science*, 27, 515-527, 1992.
- Lou, S.H., L. Tsang, C.H. Chan, and A. Ishimaru, "Application of the finite element method to Monte Carlo simulations of scattering of waves by random rough surfaces with periodic boundary conditions," *J. Electr. Waves Appl.*, 1991.
- Michel, T.R., M. Knotts, and K.A. O'Donoghue, "Stoke's matrix of a one-dimensional perfectly conducting rough surface," *JOSA*, 9, 585-596, 1992.
- Ngo, H.D., and C. Rino, "The application of beam simulation to scattering at low grazing angles Part I: III (III IOC II I E+ % and validation," submitted to *Radio Science*, 1993.
- Rice, S.O., "Reflection of electromagnetic waves from slightly rough surfaces," *Commun. Pure Appl. Math.*, vol. 4, 351-378, 1951.
- Rodríguez , E., and Y. Kim, "A unified perturbation expansion for rough surface scattering," *Radio Science*, 27, 79-93, 1992.
- Rodríguez , E., Y. Kim, and S.L. Durden, "A numerical Assessment of rough surface scattering theories: horizontal polarization," *Radio Science*, 27, 4, 497-513, 1992.
- Tsang, L., J.A. Kong, H.T. Shin, **Theory of Microwave Remote Sensing**, Wiley-Interscience, p. 102, 1985.
- Thorsos, E. I., "The validity of the Kirchhoff approximation for rough surface scattering using a Gaussian roughness spectrum," *J. Acoust. Soc. Am.*, 83, 78-92, 1988.
- Thorsos, E. I., "Acoustic scattering; from a "Pierson-Moskowitz" sea surface," *J. Acoust. Soc. Am.*, 88, 1, 335-349, 1990.
- Trizna, D.B., "Statistics of low grazing angle radar sea scatter for moderate and fully developed ocean waves," *IEEE Trans. Ant. and Prop.*, AP-39, 1(381-1690, 1991.

Veisoglu, M.E., H.A. Yuch, R. P. Shin, and J.A. Kong, "Polarimetric passive remote sensing of periodic surfaces," J. Electro. Waves Applic., 5, no. 3, 267-280, 1991.

Wetzel, L.B., "Electromagnetic scattering from the sea at low grazing angles," in Surface Waves and Fluxes, Vol. 11, G.L. Geernaert and W.J. Plant (eds.), Kluwer Academic Publishers, Dordrecht, 1990.

Figure Captions

Figure 1: Figure 1a shows the percent of the surface illuminated for surfaces whose longest wavelength is 102.4λ (empty circles); 51.2λ (full circles); 25.6λ (empty squares); and 12.8λ (full squares). Figure 1b shows the rms slope (empty circle) and rms curvature (solid circle) for the same surfaces. The spectral decay power is -3.

Figure 2: Polarimetric parameters for $\sigma_h = 0.1\lambda$, 89° incidence angle and $A = 102.4\lambda$ (crosses), $A = 51.2\lambda$ (diamonds), and $A = 25.6\lambda$ (triangles).

Figure 3: Polarimetric parameters for $\sigma_h = 1.0\lambda$, 80° incidence angle and $A = 102.4\lambda$ (crosses), $A = 51.2\lambda$ (diamonds), $A = 25.6\lambda$ (triangles), and $A = 12.8\lambda$ (squares).

Figure 4: Polarimetric parameters for $\sigma_h = 1.0\lambda$, 89° incidence angle and $A = 102.4\lambda$ (crosses), $A = 51.2\lambda$ (diamonds), and $A = 25.6\lambda$ (triangles).

Figure 5: Same as figure 4, but the surface has been filtered so that no wavelengths smaller than λ are present.

Figure 6: Source function spectrum (H polarization-triangles; V polarization-squares), HV correlation coefficient and phase difference for $\theta_0 = 89.0^\circ$ and $A = 102.4\lambda$ (a), $A = 51.2\lambda$ (b), and $A = 25.6\lambda$ (c).

Figure 7: Same as figure 6, but the surface has been filtered so that no wavelengths smaller than λ are present.

Figure 8: Horizontally polarized near field (top), evanescent field (middle), and surface current (bottom) for $\theta_0 = 89^\circ$ and a surface from the set of $A = 25.6\lambda$ surfaces.

Figure 9: Same as figure 8, but for vertical polarization.

Figure 10: Same as figure 9, but the surface has been filtered removing any components whose wavelength is smaller than λ .

Figure 11: Same as figure 9, but the incidence angle is 60° .

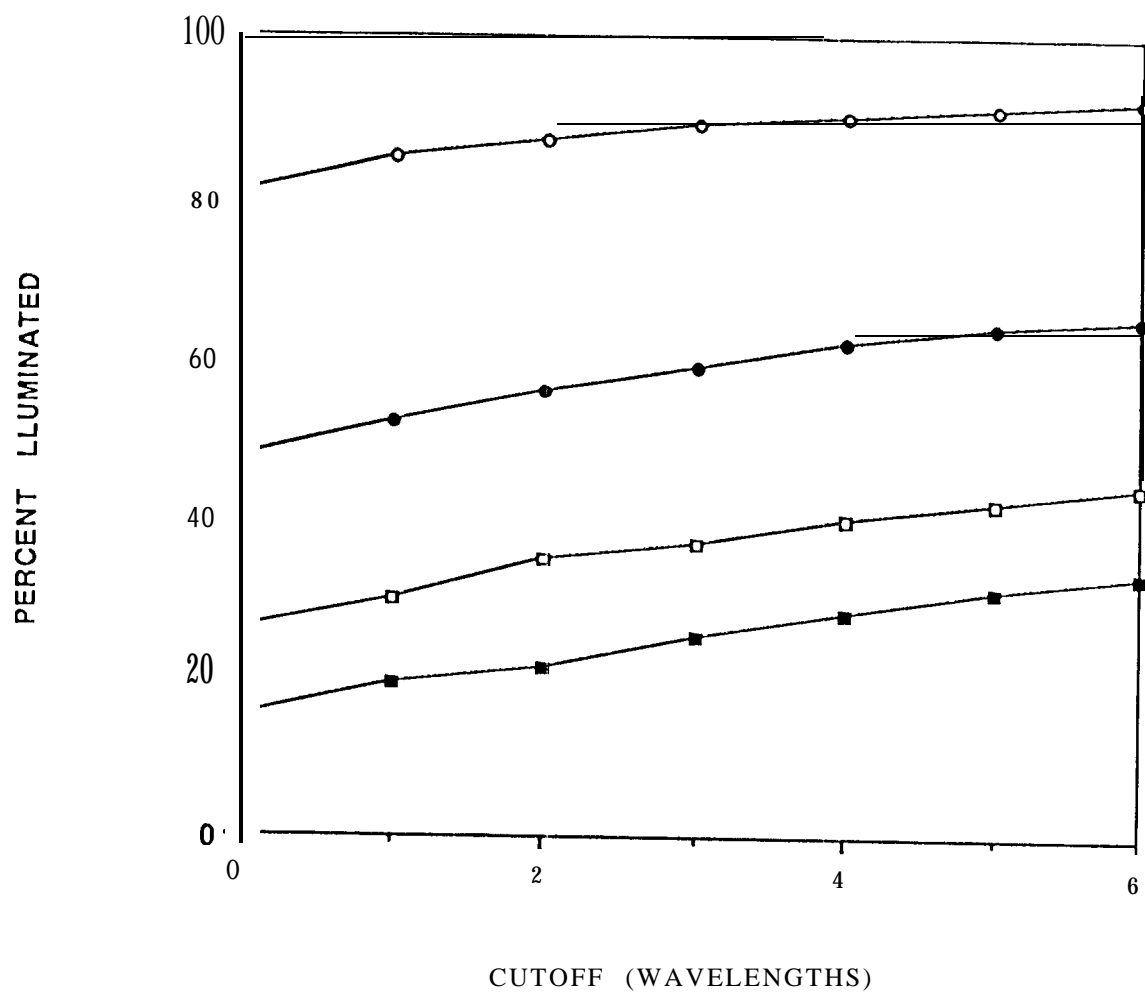


Figure 1a

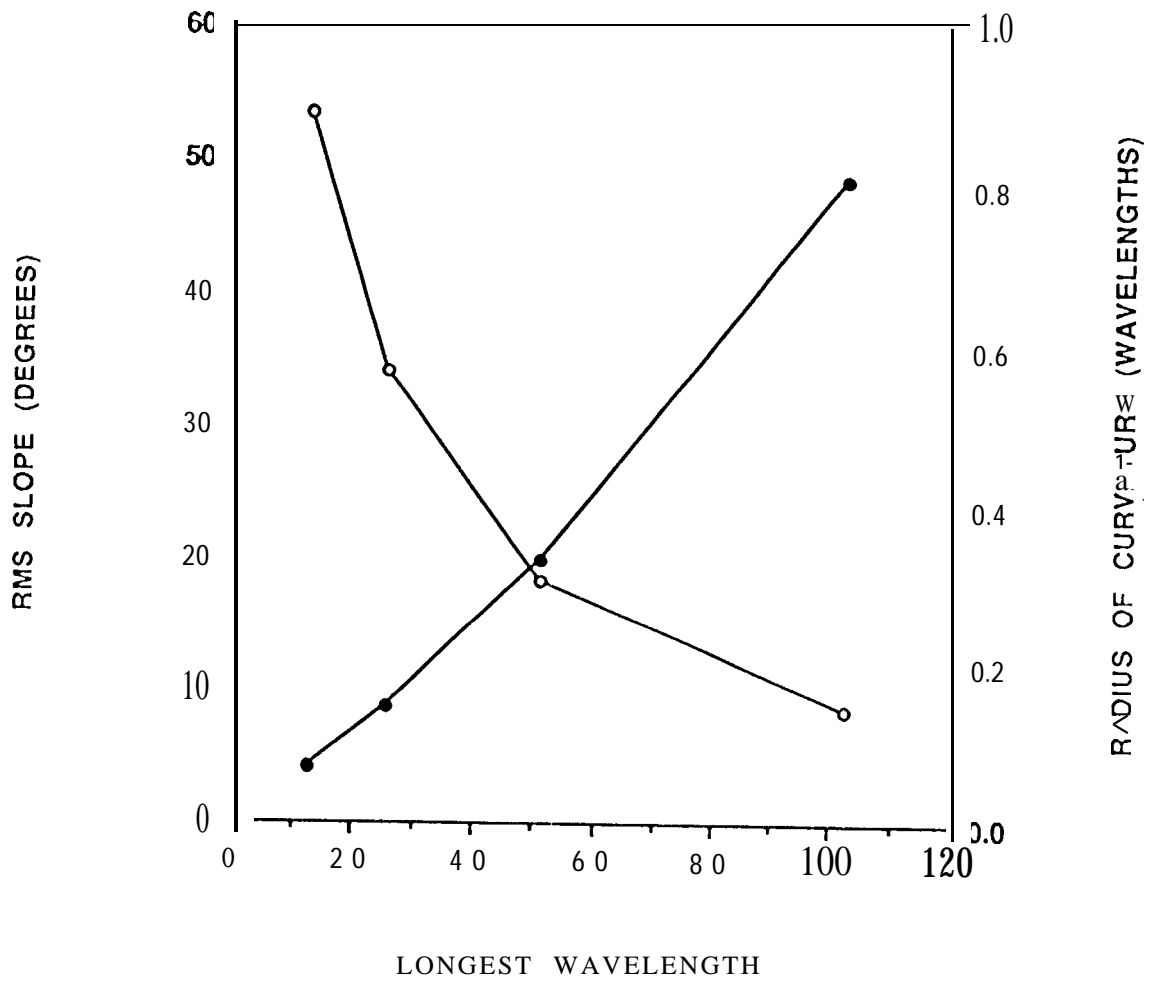
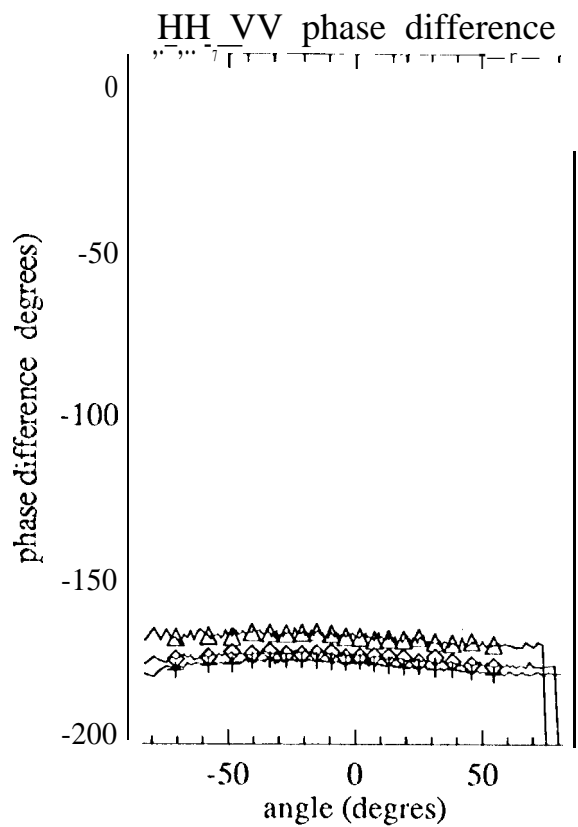
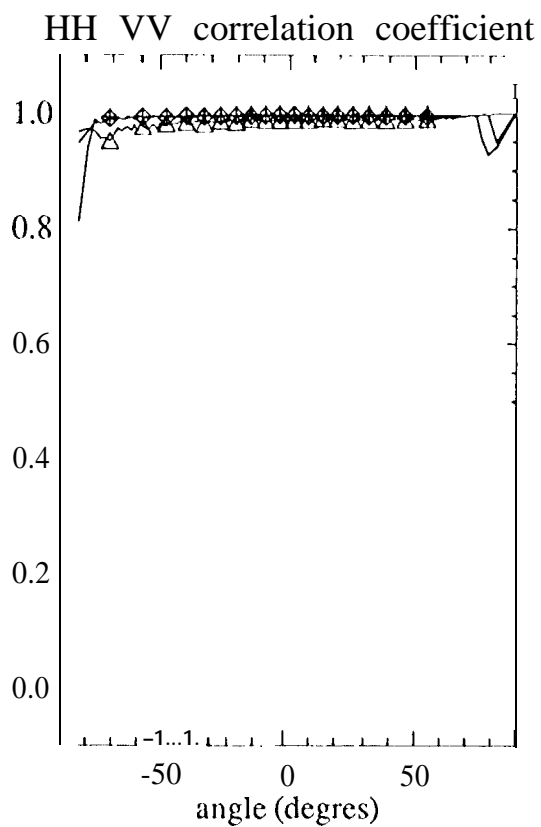
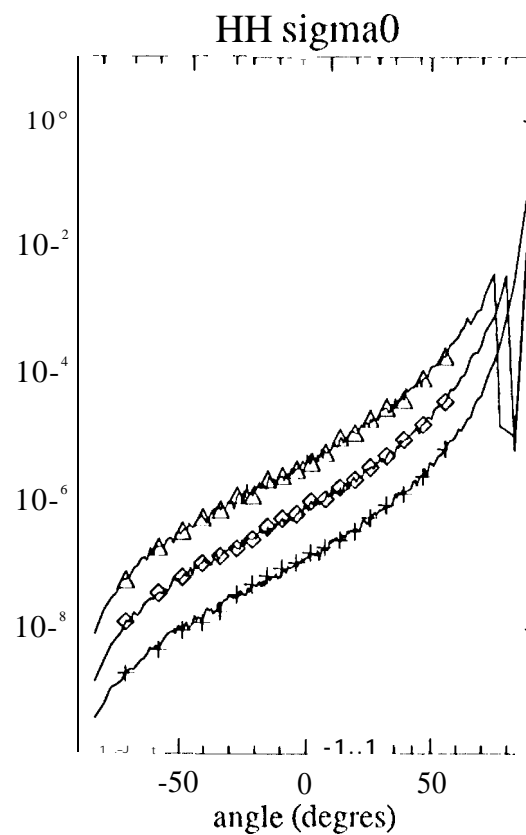
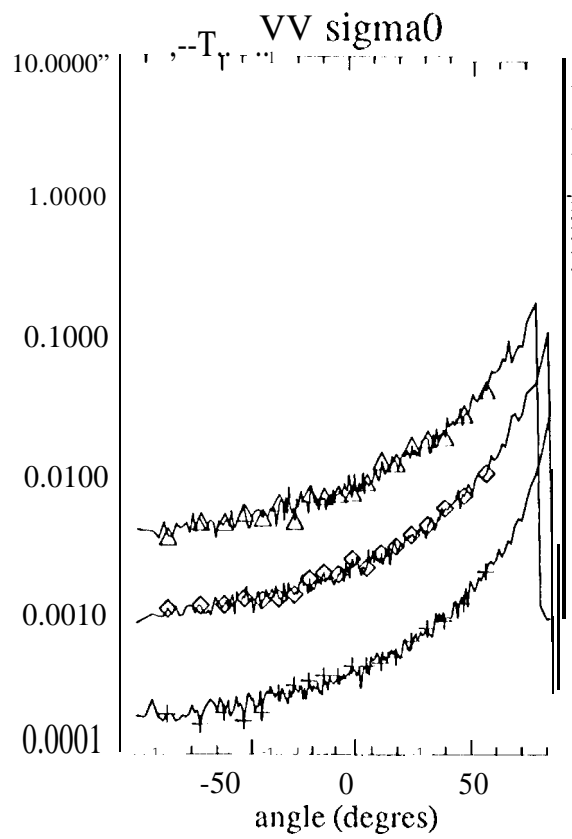
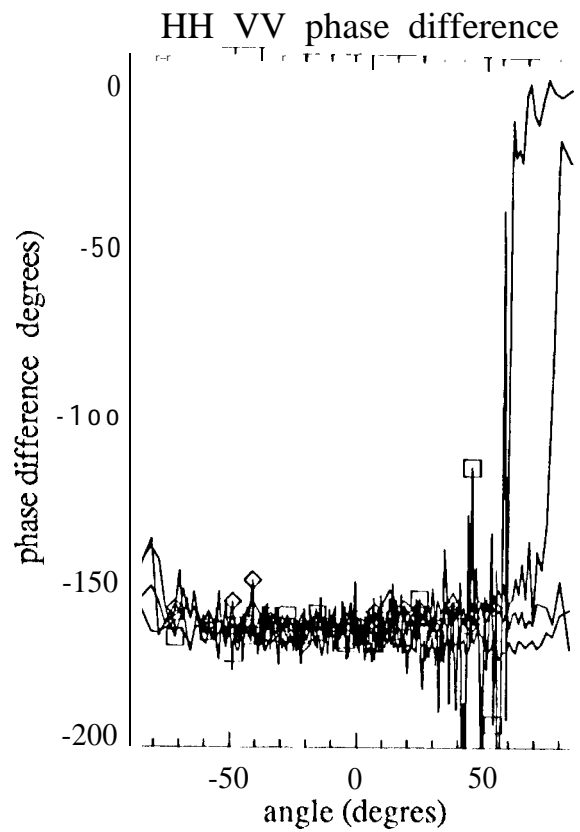
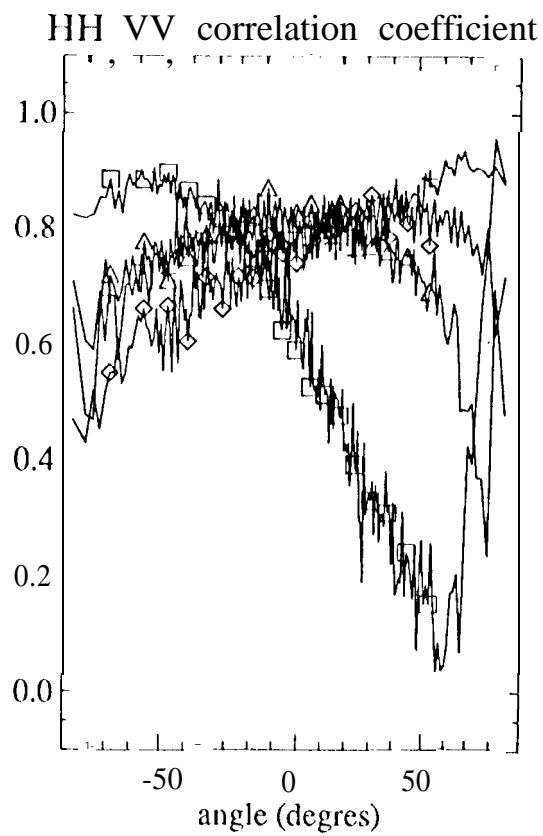
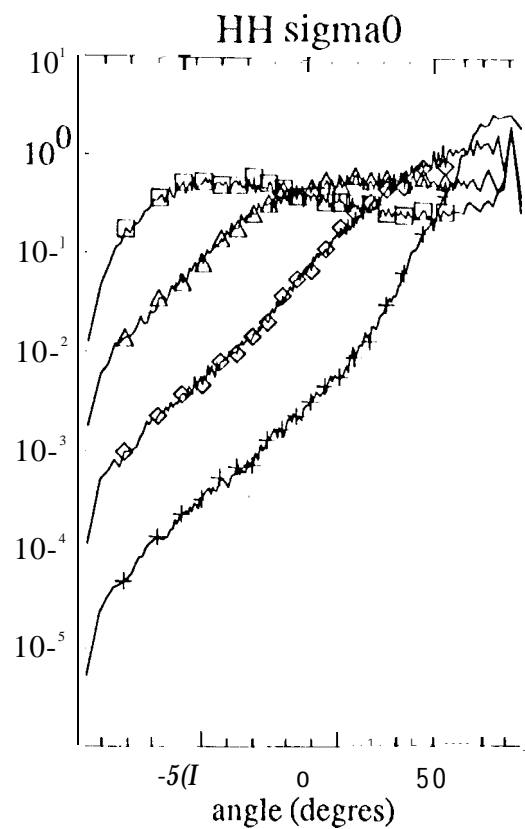
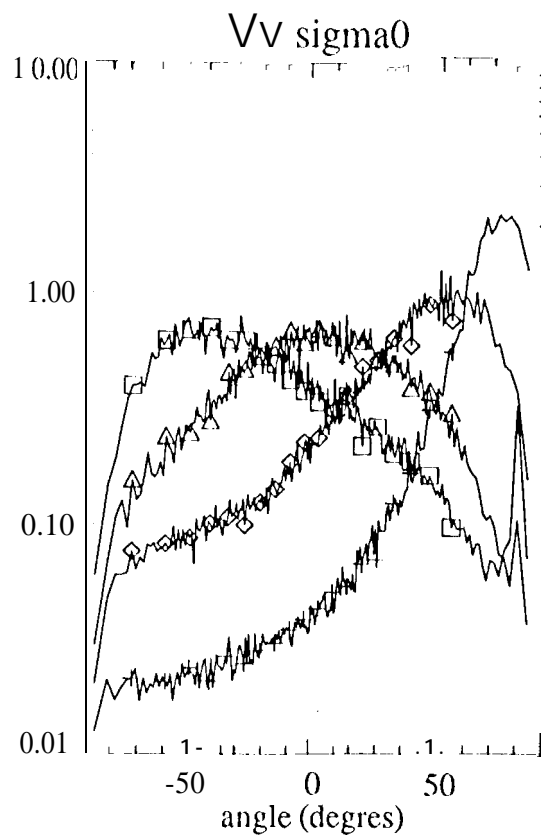
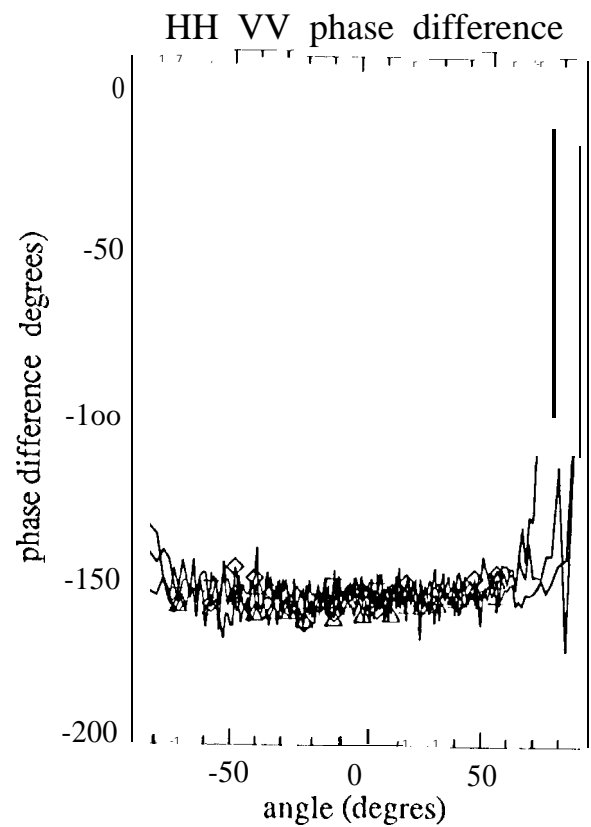
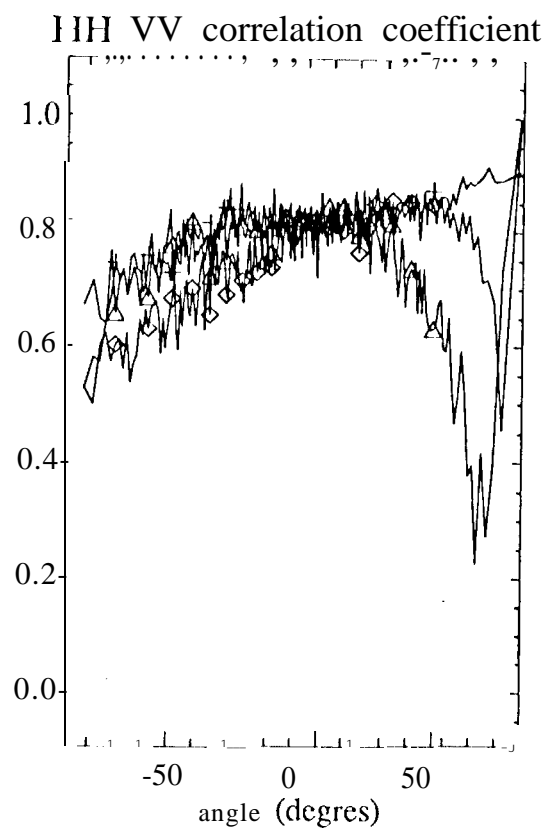
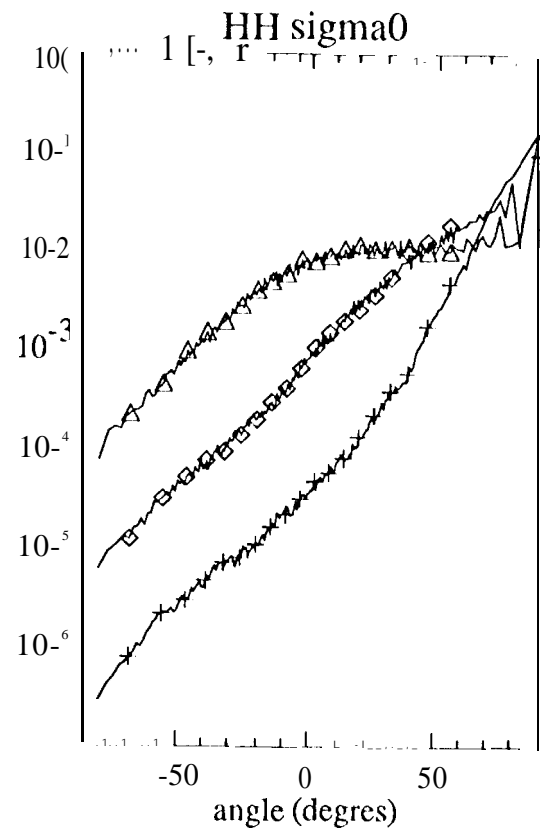
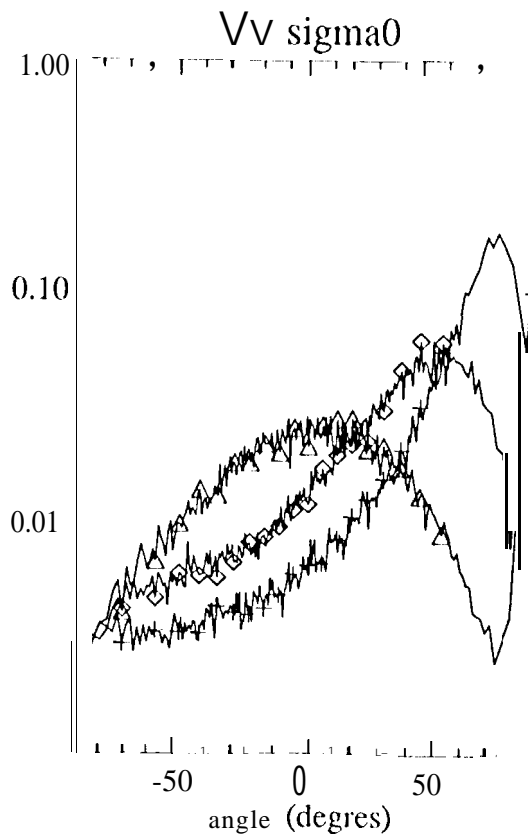
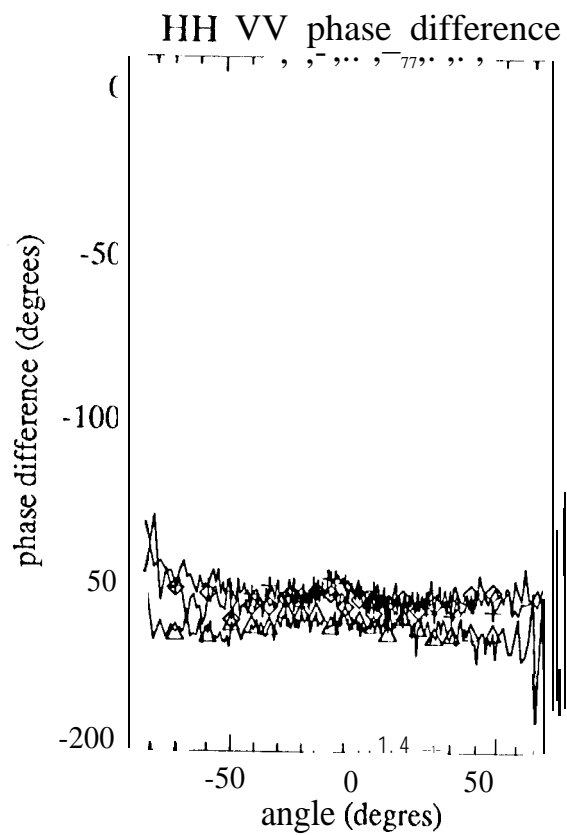
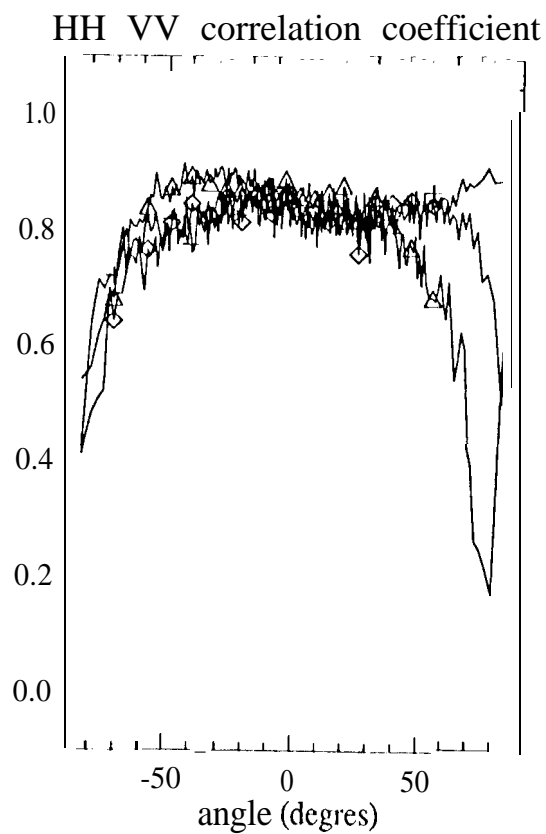
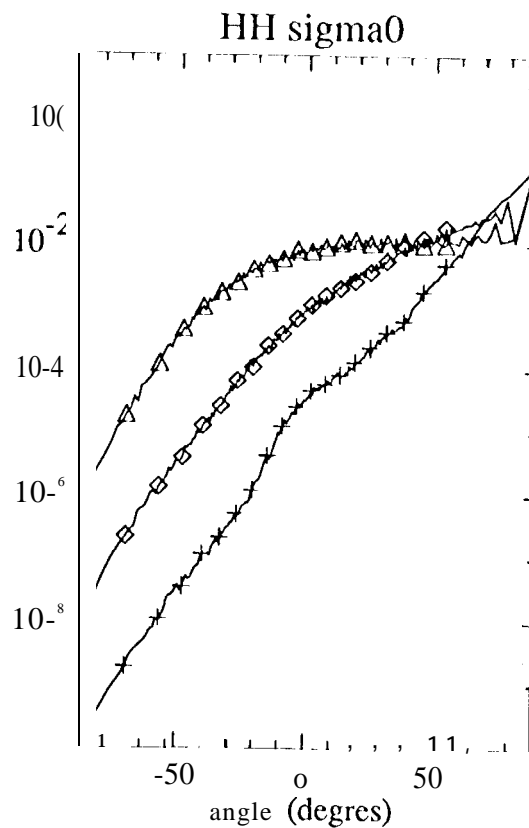
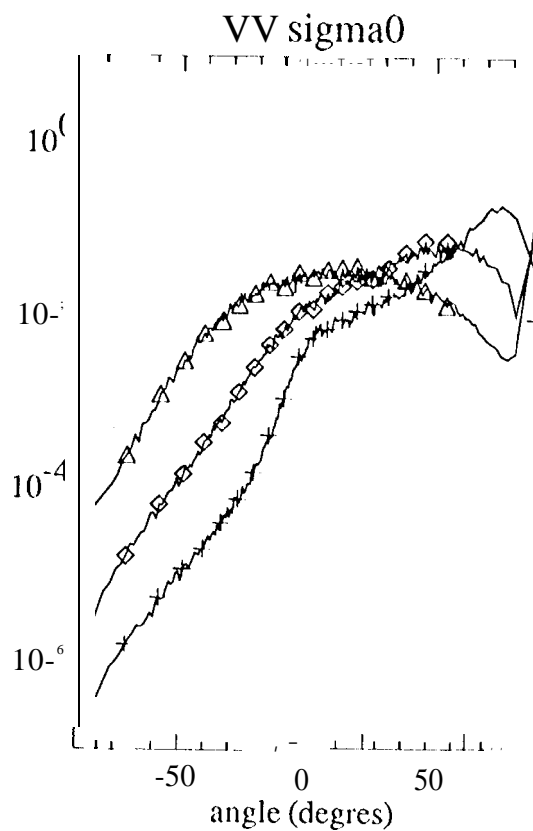


Figure 1.b

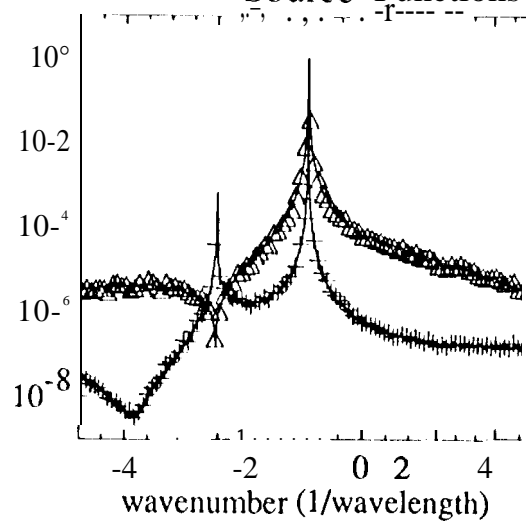




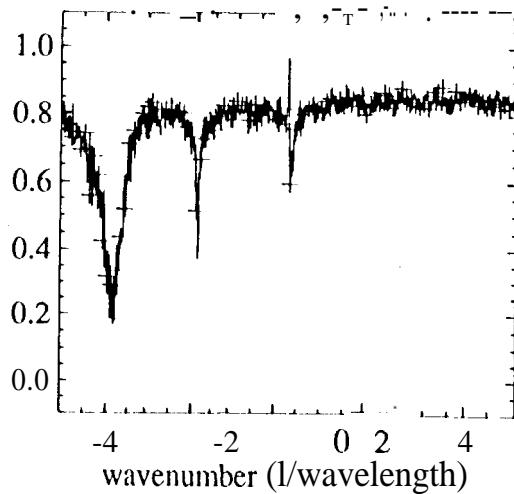




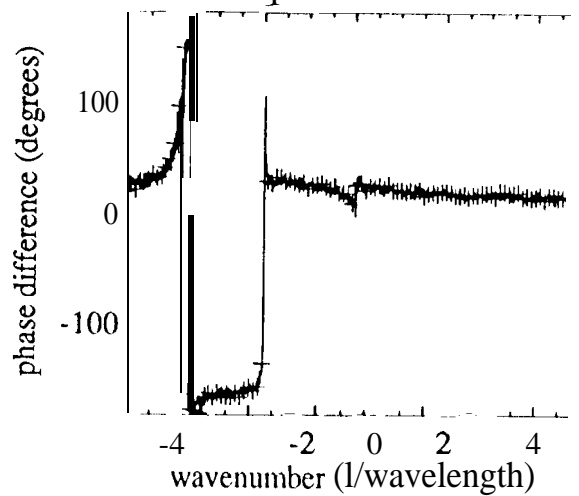
H and V Source Functions



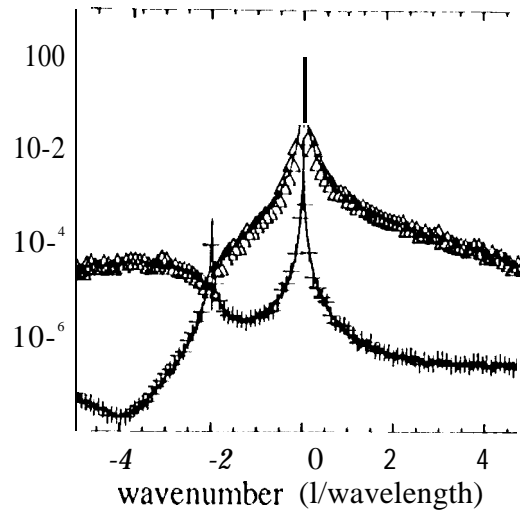
H V correlation coefficient



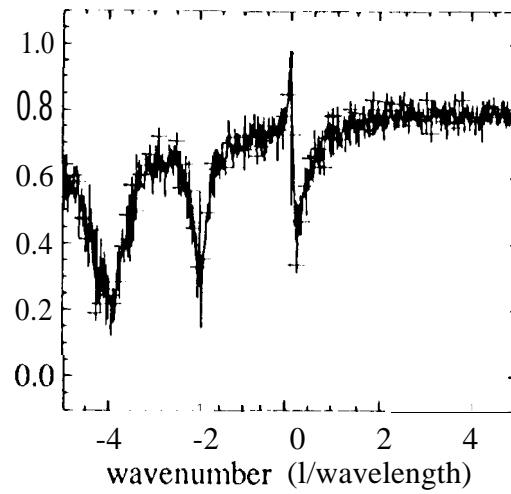
H V phase difference



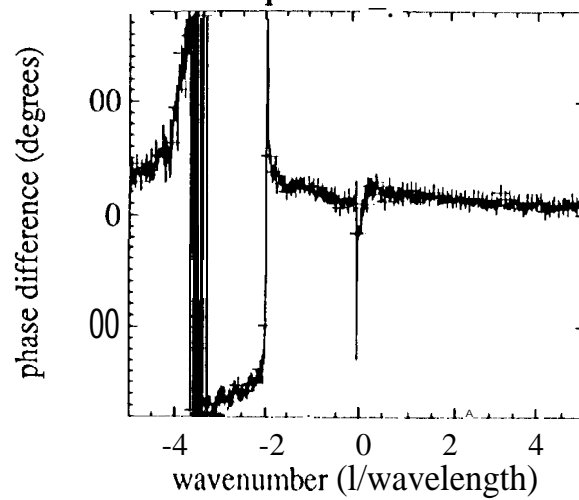
H and V Source Functions

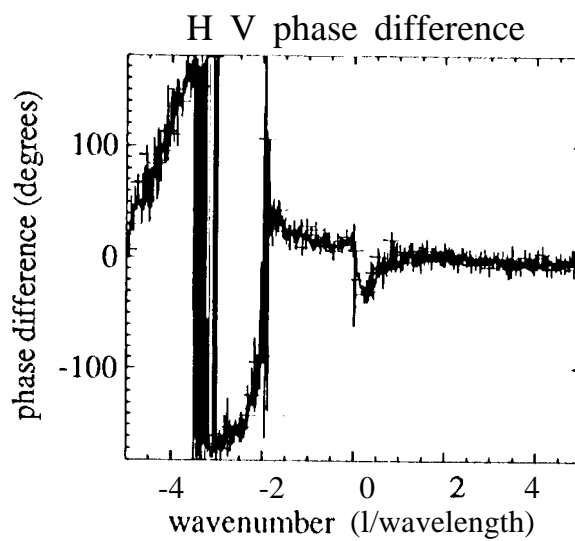
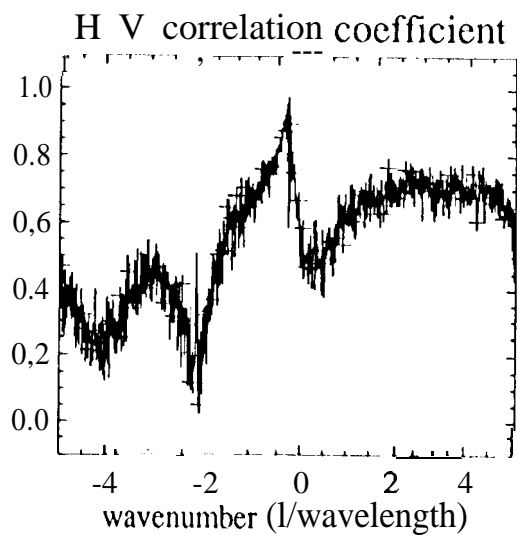
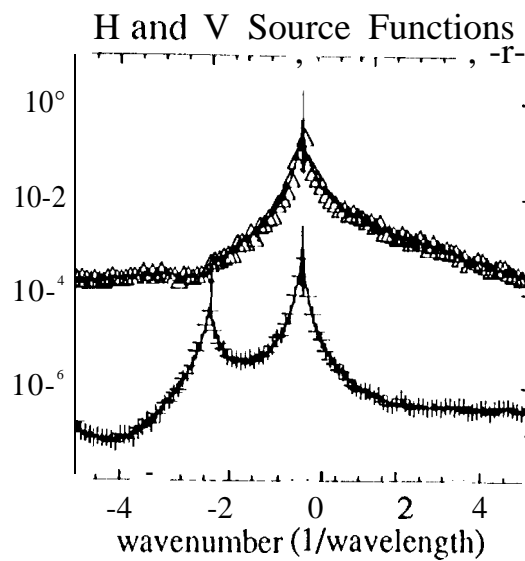


H V correlation coefficient

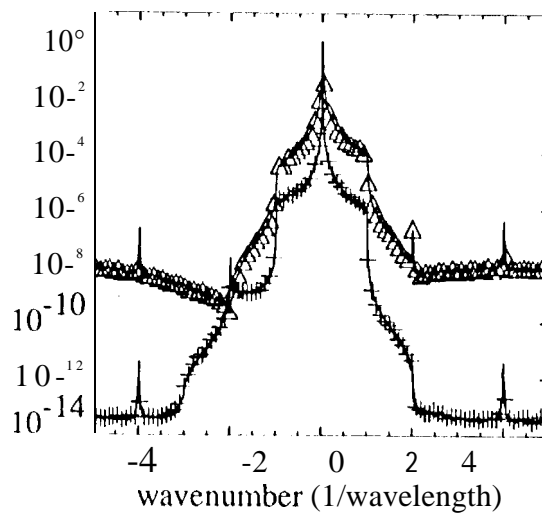


H V phase difference

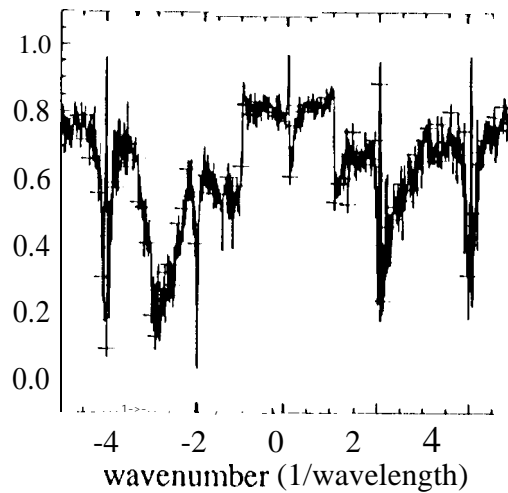




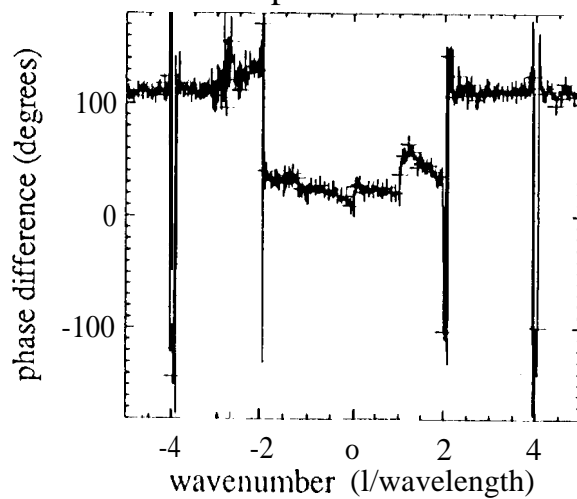
H and V Source Functions



H V correlation coefficient



H V phase difference



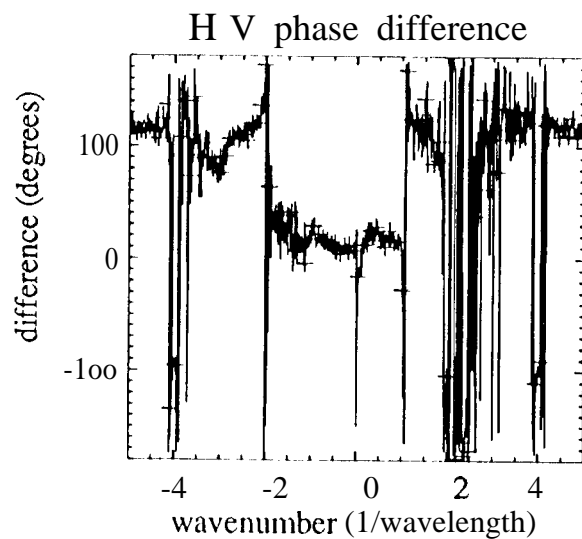
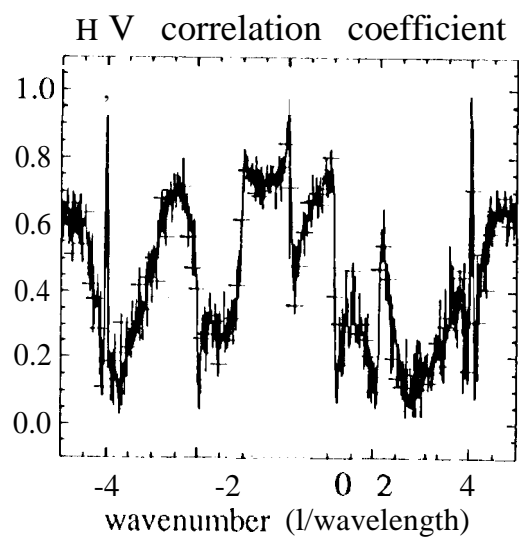
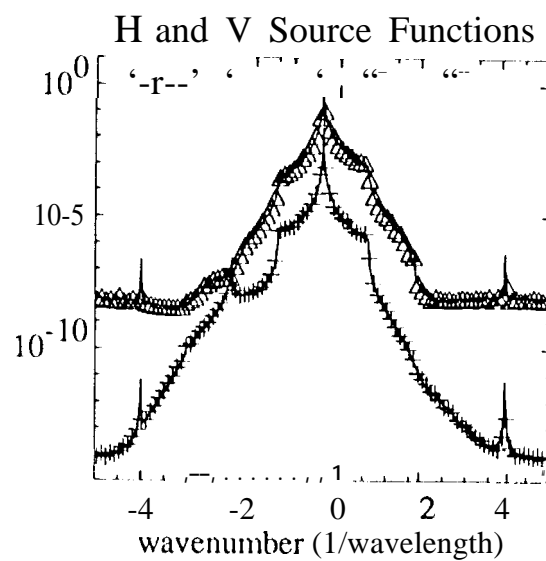
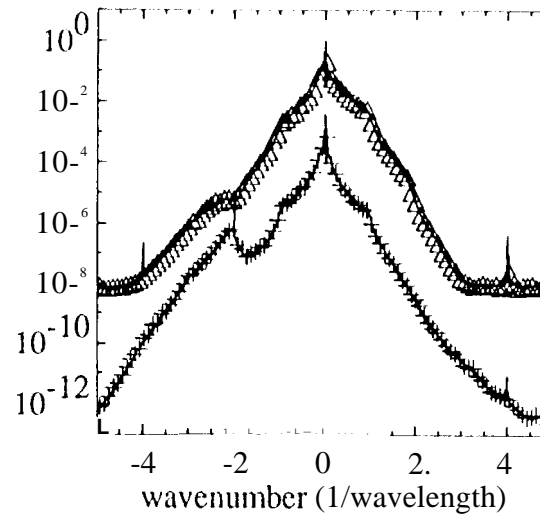
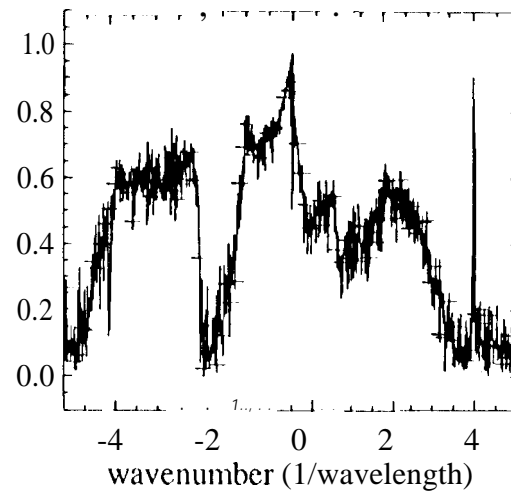


Figure 2.12

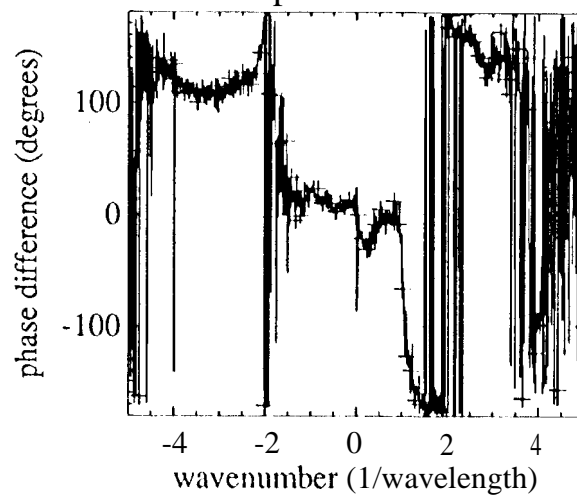
H and V Source Functions



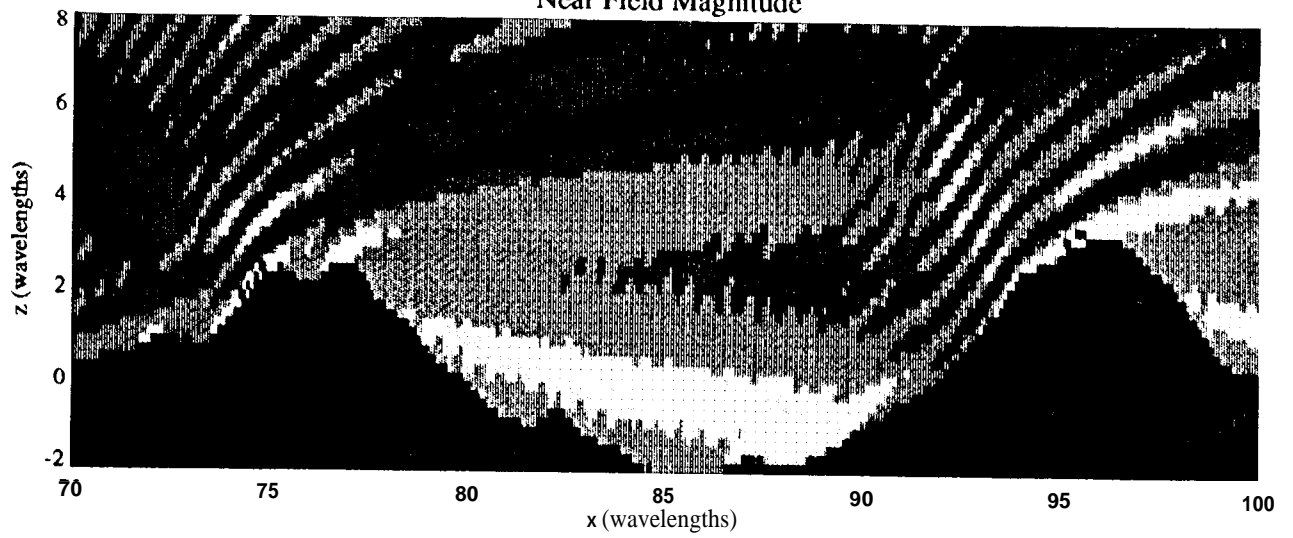
H V correlation coefficient



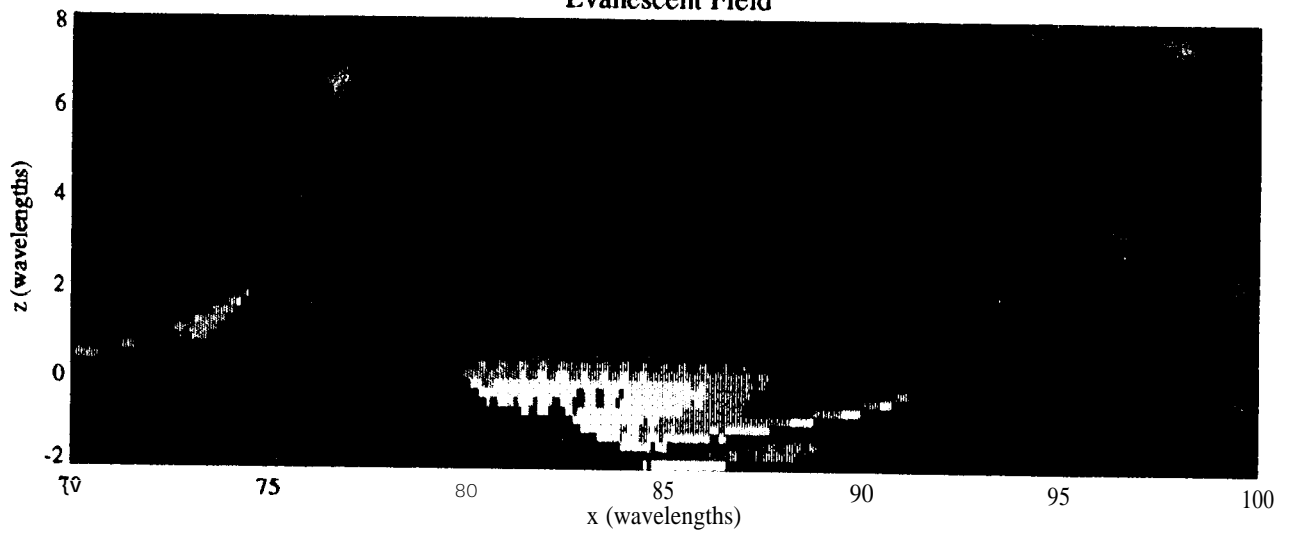
H V phase difference



Near Field Magnitude



Evanescent Field



Current Magnitude

